Uncertainty quantification and global sensitivity analysis of seismic metabarriers

Farhad Zeighami[a,*], Leonardo Sandoval[b], Alberto Guadagnini[b], Vittorio Di Federico[a]

[a] *Department of Civil, Chemical, Environmental and Materials Engineering - DICAM, University of Bologna, Viale Risorgimento, 2, Bologna, 40136, Italy*

[b] *Dipartimento di Ingegneria Civile e Ambientale, Politecnico di Milan, Piazza L. Da Vinci 32, Milan, 20133, Italy*

Abstract

Seismic metabarriers consist of an array of locally resonant elements (i.e., mechanical resonators) installed over the soil surface, whose design is rationally engineered to reduce ground-induced vibrations and shield vulnerable structures against seismic surface waves. Successful design and implementation of seismic metabarriers require a comprehensive knowledge and characterization of the role played by the model parameters (and their associated uncertainty) governing soil-barrier dynamic interaction. In this context, sensitivity analysis techniques allow assessing the response of a given model through the quantification of the influence and action of model inputs (and model input uncertainties) concerning a target model output. This study relies on global sensitivity analysis techniques to investigate the influence that the uncertainty associated with three key mechanical parameters of a metabarrier (i.e., soil density, soil shear modulus, and mass of mechanical resonators) has on its seismic isolation performance. The latter is measured in terms of transmission coefficient (TC). We do so by employing a two-dimensional wave finite element model developed under the plane-strain conditions to evaluate the dispersion relation and transmission coefficient of a metabarrier interacting with Rayleigh waves in the low-frequency regime (i.e., frequencies between 2Hz and 7Hz). Our results suggest that the shear modulus is the uncertain parameter with the most significant influence on the transmission coefficient of the metabarrier across the entire frequency range of interest. Otherwise, the resonator mass plays a substantial role in the frequency range close to the metabarrier resonant frequency.

*Corresponding author: Farhad.zeighami3@unibo.it

Keywords: Seismic metamaterials, Metabarrier, Seismic surface waves, Global sensitivity analysis, Surrogate modeling, Polynomial chaos expansion.

1. Introduction

Elastic metamaterials are artificial composite structures designed to possess unconventional mechanical properties (Deymier et al., 2013). Since their emergence around two decades ago, elastic metamaterials have found several applications in mechanical and civil engineering fields. In the context of earthquake engineering, seismic metamaterials (SMs) are proposed as an innovative isolation technique to safeguard critical and vulnerable structures such as high-rise buildings, urban areas, historical places, and heritage sites (Brûlé et al., 2014; Krödel et al., 2015; Colombi et al., 2016c; Miniaci et al., 2016). SMs are generally classified according to their application, regulation mechanisms, and arrangement patterns (Mu et al., 2020). From an application perspective, SMs are categorized as periodic (Cheng and Shi, 2013; Cheng et al., 2020) and resonant foundations (Basone et al., 2019; Sun et al., 2019) that interact with seismic waves to shield unprotected residential buildings and industrial facilities, as well as periodic (Huang and Shi, 2013; Ni and Shi, 2022) and resonant barriers (Palermo et al., 2016; Colombi et al., 2017) to protect critical infrastructures or structures against incident surface waves. Among these systems, locally resonant barriers, namely metabarriers, incorporate wave-impeding devices with feasible dimensions from an engineering attitude that do not require any structural intervention to the target infrastructure.

A seismic metabarrier is a passive resonant barrier organized as an arbitrary arrangement of resonant structures/units with dimensions much smaller than the wavelength of seismic waves (Palermo et al., 2016). Metabarriers are typically installed in the vicinity of target structures and activated by the motion of incoming waves. The operating resonant frequency of a metabarrier is usually tuned in the low-frequency regime (i.e. below 10 Hz), where most of the elastic energy of seismic waves exists (Colombi et al., 2016c; Palermo et al., 2016, 2018b). The dynamic interaction between metabarrier and seismic waves is described analytically through the effective medium approach (Boechler et al., 2013) and the multiple scattering theory (Pu et al., 2021) and further assessed through finite element (FE) numerical analyses (Palermo et al., 2018b; Zeighami et al., 2019). The attenuation performance of a metabarrier was verified in small-scale laboratory tests for shear vertical (Palermo et al., 2016; Zaccherini et al., 2020a) and shear horizontal surface waves (Zaccherini et al., 2020b). Since then, metabarriers have been associated with various applications in waveguiding (Maznev and Gusev, 2015), wave filtering (Colombi

et al., 2016c), wave focusing (Colombi et al., 2016b), and energy harvesting (De Ponti et al., 2020).

After the introduction of the metabarrier concept in civil and material engineering communities, various design strategies have been proposed to enhance their efficiency in terms of seismic wave attenuation. These include the exploitation of mechanical oscillators (Palermo et al., 2016), resonant pillars (Colombi et al., 2016a), or locally resonant inclusions (Zeighami et al., 2021a) as the fundamental unit of metabarriers. Several studies are then keyed to the assessment of optimal spatial arrangement of mechanical resonators. These resonant elements can be either installed at the soil surface (Boutin and Roussillon, 2006) or buried inside soil layers (Zaccherini et al., 2020a; Zeighami et al., 2021a). To the best of our knowledge, previous literature studies evaluate the seismic wave attenuation associated with the metabarriers by considering their design parameters as deterministic quantities. Otherwise, in the context of geophysical sciences, various types of uncertainties are associated with the soil system and mechanical resonators. Henceforth, the aim of this research is two-fold: (*i*) to identify the uncertain parameters of the coupled soil-barrier dynamic system, and (*ii*) to quantify the influence of these uncertain parameters on the surface wave attenuation performance of metabarriers measured as the transmission coefficient (TC).

In this work, we employ global sensitivity analysis (GSA) techniques to quantify the influence of the uncertainties associated with the mechanical properties of metabarrier components on the seismic wave attenuation of the latter. We rely on (*i*) the classical variance-based Sobol indices, which quantify the expected reduction of a model output variance due to the knowledge of (or conditioning on) a parameter value, and (*ii*) the moment-based AMA indices, which quantify the normalized expected deviation of the statistical moment of a model output due to the knowledge of (or conditioning on) a parameter value. Sobol indices are broadly used in structural engineering problems, including for instance load-carrying capacity analysis of steel plane frames (Kala, 2011) and axial load evaluation of tie-rod elements (De Falco et al., 2021). AMA indices (termed after the initials of the authors) have been recently proposed by Dell'Oca et al. (2017). These global sensitivity metrics recognize that the uncertainty of a model parameter can be imprinted onto diverse statistical moments of model outputs. They have been applied to quantify uncertainty in different civil engineering scenarios, including degradation of contaminants in soils (la Cecilia et al., 2020), groundwater flow (Bianchi Janetti et al., 2019), and gas flow in low permeable materials (Sandoval et al., 2022). In the context of geotechnical and earthquake engineering, other global sensitivity analysis techniques have been employed for uncertainty quantification of layered periodic foundations (Liu et al.,

2020), offshore wind turbine foundations (Velarde et al., 2019), and ground motion modeling in seismic risk assessment (Vetter and Taflanidis, 2012).

Successful application of GSA techniques typically requires multiple evaluations of the model to be analyzed. In cases where such evaluation is associated with a heavy computational burden, applying GSA may become unfeasible (Sudret, 2008). In such a case, using a reduced complexity model minimizes the computational burden associated with the evaluation of the model whilst preserving the relationships between the inputs and outputs of the model (Dell'Oca et al., 2017). In this study, we rely on polynomial chaos expansion (PCE) to construct models of reduced complexity, our approach being otherwise fully compatible with other model reduction techniques. PCE-based techniques have been widely employed in studies to quantify uncertainty in diverse civil engineering areas such as dam engineering (Hariri-Ardebili and Sudret, 2020), hydraulic fracturing operations (Gläser et al., 2016), and CO_2 sequestration (Zhang and Sahinidis, 2013).

The paper is structured as follows: first, the analytical expression underlying the design of seismic metabarriers is given in Sec. 2.1. A two-dimensional Finite Element (FE) model of the metabarrier basic module is developed in Sec. 2.2 to demonstrate the dispersive features of a single resonator. Then, a full numerical model of the entire barrier is realized to assess its seismic isolation efficiency in Sec. 2.3. Next, uncertain model parameters influencing the attenuation efficiency of a metabarrier are introduced in Sec. 2.4. Secs. 2.5 and 2.6 describe the GSA and surrogate modeling techniques employed in the study. The accuracy of the surrogate models, as well as the results of the GSA, are presented in Sec. 3. Finally, conclusions and future research directions are addressed in Sec. 4.

2. Methodology and materials

In this Section, we explain the design methodology of a locally resonant metabarrier rationally engineered to impede the propagation of seismic surface waves. Metabarriers are composed of a series of passive mechanical resonators organized in a regular grid with identical spacing to be directly placed over the soil surface. The metabarrier is installed in the proximity of a target structure/infrastructure and activated by the motion of incoming waves. The dynamic coupling between a seismic metabarrier and vertically-polarized seismic waves (also called Rayleigh waves) is studied analytically via a closed-form dispersion law proposed by Palermo et al. (2016), where resonators are assumed to have a linear elastic behavior and the soil is modeled as an isotropic and homogeneous half-space. In this dynamic system, the exchange of stress between

resonators and the soil generates a low-frequency band gap (BG) in the frequency spectrum of surface waves, where a significant ground-motion attenuation is expected (Colquitt et al., 2017). The band gap width depends on the operating frequency and mass per unit area of the resonators (Palermo et al., 2016). Since no surface mode can propagate within the band gap frequency region, the elastic energy of the seismic waves diverges from the soil surface trajectory to the bulk media (Colquitt et al., 2017).

Recently, more complex theoretical models have been developed to account for the soil heterogeneity (Zeng et al., 2022) and its non-linear behavior (Kanellopoulos et al., 2022), as well as exploiting non-linear resonators inside the metabarrier arrangement (Palermo et al., 2022). For the case of stratified soil, the emergence of the band gap in the dispersion relation is discarded by the propagation of higher-order surface modes. Thus, surface-to-shear wave conversion is hindered. However, a substantial ground motion reduction is observed around the collective resonant frequencies of the resonators (Palermo et al., 2018a; Zeng et al., 2022). These additional complexities are usually ignored in the long-wavelength (low-frequency) regime to develop theoretical frameworks that capture the fundamental physics of wave propagation settings. Hence, we resort to a linear elastic resonator and a linear, homogeneous, and isotropic soil model in this study.

The overall workflow and research methodology are depicted in Fig. 1 and discussed extensively in the following. We first present the analytical dispersion law for the seismic metabarrier. We then illustrate the seismic isolation assessment of the barrier through a surrogate model and by a global sensitivity analysis of the uncertain parameters.

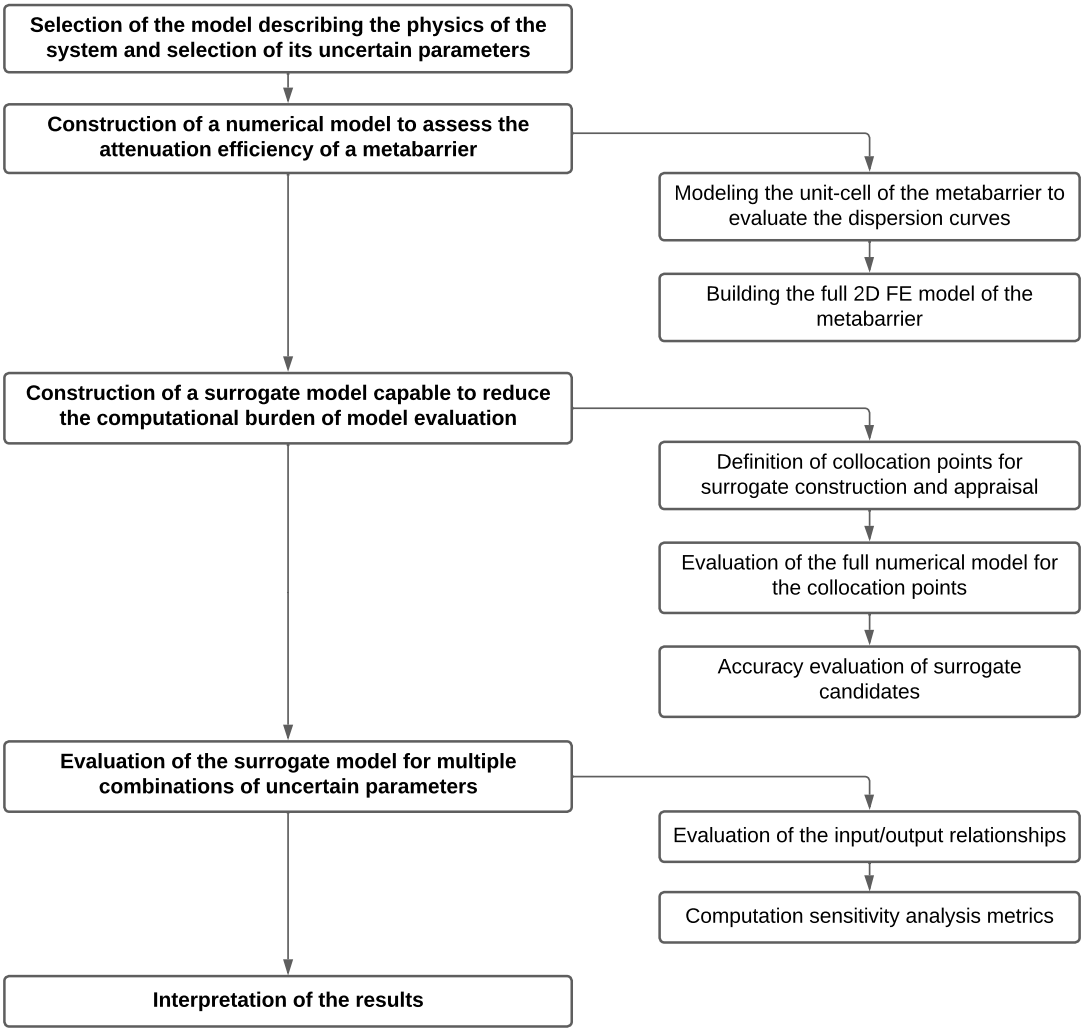

Figure 1: Global sensitivity analysis framework used to assess seismic isolation performance of a compact seismic metabarrier.

2.1. Analytical dispersion relation of seismic metabarriers

We study Rayleigh wave propagation through an elastic half-space equipped with a finite-size array of surface resonators, as shown in Fig. 2. Rayleigh waves are propagating in the x-direction, while they are polarizing in the z-direction. We note that parameters related to resonator and soil are denoted with subscription r and s, respectively. The resonators have a length of a_r and an out-of-plane depth of l_r

that assumes a unit value in a 2D problem. As such, the resonators have dimensions much smaller than the wavelength of surface Rayleigh waves, i.e. $a_r << \lambda_{RW}$, and they are distributed in a regular arrangement with an equal spacing of a_r, identical to the resonator length. Hence, the resonator influence area is $A_r = a_r \times l_r$.

The half-space is constituted by an isotropic and homogeneous soil with density ρ_s, Poisson's ratio ν_s, Young's modulus E_s, and shear modulus $G_s = E_s/(2(1+\nu_s))$. Each resonator of the metabarrier has a mass m_r linked to the soil surface via linear elastic springs with axial stiffness K_r. Relying on a 2D instead of a 3D model can enable one to capture the main physics of resonator-soil coupling scenarios (see, e.g. (Palermo et al., 2016; Colquitt et al., 2017; Palermo et al., 2018b)).

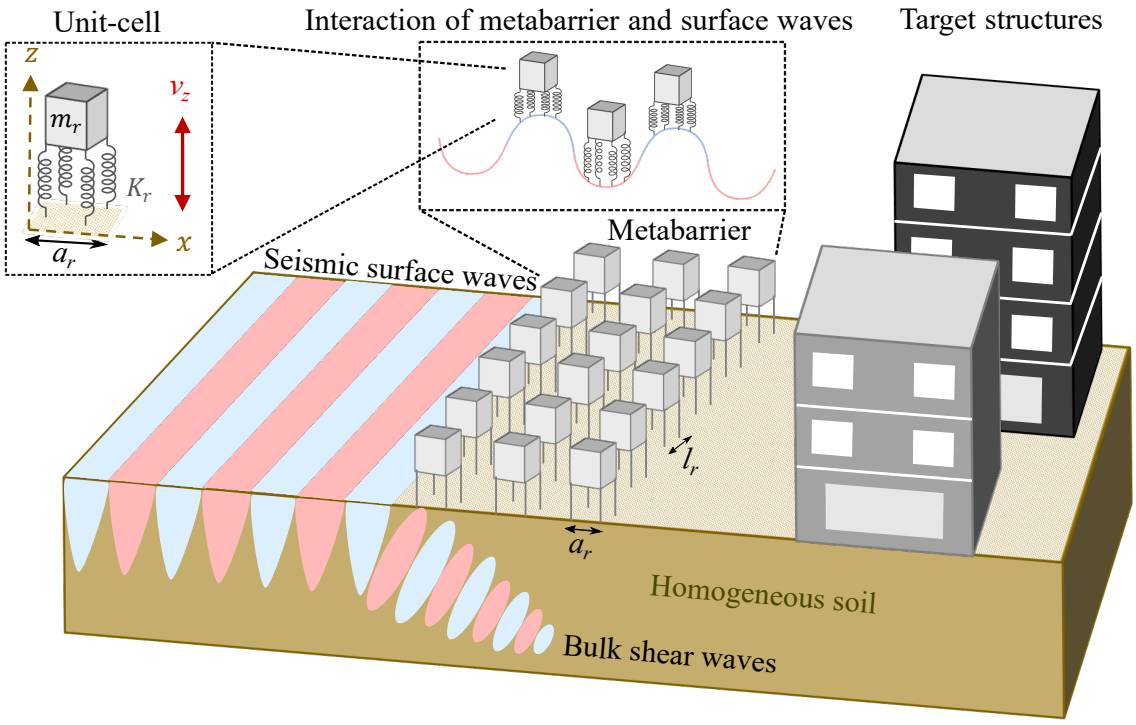

Figure 2: Schematic of a seismic metabarrier composed of surface resonators interacting with incoming seismic surface waves. The inset shows a unit-cell of the metabarrier consisting of a rigid mass and four elastic springs.

The interaction between the sub-wavelength resonators of a metabarrier, the elastic soil domain, and surface Rayleigh waves is defined via the effective medium approach (Maznev and Gusev, 2015). According to the latter, a metabarrier can be seen as a thin resonant boundary layer that exerts uniform vertical stress on the soil

surface. This approximation allows for deriving a dispersion law (i.e., the relationship between the wavenumber and frequency space) that predicts the fundamental dispersive features of metabarriers and guides their design procedure. We exploit the dispersion relation originally developed by Boechler et al. (2013), and update it in terms of the elastic modulus of a homogeneous soil and of the mechanical parameters of the resonators as:

$$\left(\frac{m_r\omega^2}{K_r}-1\right)\left[\left(2-\frac{\rho_s\omega^2}{G_sk^2}\right)^2-4\sqrt{1-\frac{\rho_sC^2\omega^2}{G_sk^2}}\sqrt{1-\frac{\rho_s\omega^2}{G_sk^2}}\right]=\frac{m_r\rho_s}{a_rl_rG_s^2}\frac{\omega^4}{k^3}\sqrt{1-\frac{\rho_sC^2\omega^2}{G_sk^2}}, \tag{1}$$

where $\omega = 2\pi f$ [rad/s] represents angular frequency, f [Hz] is frequency, k [rad/m] is a wavenumber vector that can vary from 0 to the edge of the first Brillouin zone (i.e., π/a_r), and $C = \sqrt{(1-2\nu_s)/(2-2\nu_s)} = c_T/c_L$ is a dimensionless quantity expressing the ratio between the shear and longitudinal wave velocities. The dispersion relation can be formulated either in terms of Lamé parameters by exploiting the expressions $\mu = G_s$ and $\lambda = 2G_s/(1-2\nu_s)$ or via the longitudinal and shear wave speeds, whose expressions are given in Eqs. (2).

$$c_L=\sqrt{\frac{2G_s(1-\nu_s)}{\rho_s(1-2\nu_s)}},\quad c_T=\sqrt{\frac{G_s}{\rho_s}}. \tag{2a-b}$$

Eq. (1) shows that the wavenumber (k) is a function of the frequency (f), the mechanical parameters of the resonator (m_r, a_r, l_r, K_r), and the soil parameters (ρ_s, G_s, ν_s). For the sake of completeness, the dispersion relation (Eq. (1)) is recast in a dimensionless format in Appendix A.

2.2. Numerical assessment of the metabarrier through a Wave Finite Element Method

Our study relies on the Wave Finite Element Method (WFEM), initially proposed by Mace and Manconi (2008) and further developed by Palermo et al. (2018b) to assess the ground vibration attenuation capability of locally resonant metabarriers. The WFEM rests on the conventional finite element model of a small portion of the composite waveguide (namely the unit-cell) to quantify its dynamic response against incoming waves. So far, this method has been applied to various composite structures such as beams, pipes, laminated plates, sandwich panels, and thin-walled structures. The efficiency of the WFEM for the case of seismic surface wave propagation through a finite-length barrier placed on top of a soil column has been assessed in recent

studies (Zeighami et al., 2019, 2021b,a; Palermo et al., 2022). According to WFEM, a numerical model of a single resonator linked to a 2D soil column can be envisaged to satisfy the analytical dispersion law of Eq. (1). Such an approach allows modeling the entire barrier to evaluate its seismic isolation performance. The coupled resonator-soil column represents a unit-cell (fundamental module) of the barrier. The dynamic response of a finite-size chain of unit-cells obtained from frequency domain analysis yields the numerical dispersion curves. The accuracy of the developed FE model will then be verified against analytical solutions of Eq. (1).

We develop a two-dimensional FE model of a metabarrier unit-cell according to a realistic engineering design of a metabarrier. The unit-cell (see Fig. 3a) consists of a rigid mass (m_r) attached to a soil column via two vertical elastic springs, each having an axial stiffness of $K_r/2$. The length of the soil column is being taken to coincide with the resonators' spacing, a_r. The soil depth is considered large enough to mimic a semi-infinite soil media as $3\lambda_0$, where $\lambda_0 = c_R/f_r$, c_R is the Rayleigh wave velocity, and $f_r = (1/2\pi)\sqrt{K_r/m_r}$ is the resonant frequency of the resonators. The vertical and horizontal displacements of the soil bottom are restricted to avoid any undesirable motion. The horizontal displacement of the resonator mass is suppressed while the springs are allowed to elongate and compress along their vertical axis. Bloch periodicity conditions (Brillouin, 1946) are imposed on the lateral edges of the soil column to construct the numerical dispersion curve. The resonator mass and soil domain are discretized via triangular mesh elements with a minimum dimension $L_m = \lambda_0/10$. Each spring is represented by a single truss element with one node at each joint. We seek the eigenfrequency solutions of the unit-cell in the wavenumber interval of $k = [0, \pi/a_r]$.

2.3. Application to a finite-size metabarrier attached to different homogeneous soil layer

We implement WFEM on a compact metabarrier to assess its seismic surface waves isolation efficiency. The proposed metabarrier is composed of a finite number of equidistant resonators distributed over a total length λ_0 which is equivalent to an array of 20 unit-cells with an equal spacing $a_r = 1\,\mathrm{m}$ (see Fig. 3b). We note that this is the minimum length of the barrier enabling one to detect the attenuation effect. Increasing the length of the barrier (or, conversely, the number of resonators) would result in an enhanced attenuation (Pu et al., 2021). The full 2D model of the barrier is developed on the basis of the reduced numerical model of the unit-cell (see Fig. 3a); its height is equal to the depth of unit-cell ($3\lambda_0$) and has a total length of $18\lambda_0$, as shown in Fig. 3c. A harmonic input source excites the entire domain. The left part of the domain represents a reference soil (i.e., soil without metabarrier), whereas the

right side of the domain includes the metabarrier zone. The metabarrier is placed at a distance of $5\lambda_0$ from the input source to eliminate near-source effects. Both bottom corners of the soil domain are fixed to maintain the static stability of the model during simulations. In addition, Low-Reflective Boundary (LRB) conditions are imposed on the lateral and bottom edges of the model to minimize the back-reflection of surface waves from the boundaries. The barrier response is extracted from an output region with a length $L_{out} = \lambda_0$ placed after the metabarrier zone, namely barrier output. The same quantity is measured for the reference soil from the left part of the model (see soil output in Fig. 3c) to compare the soil response equipped with resonators with bare soil condition.

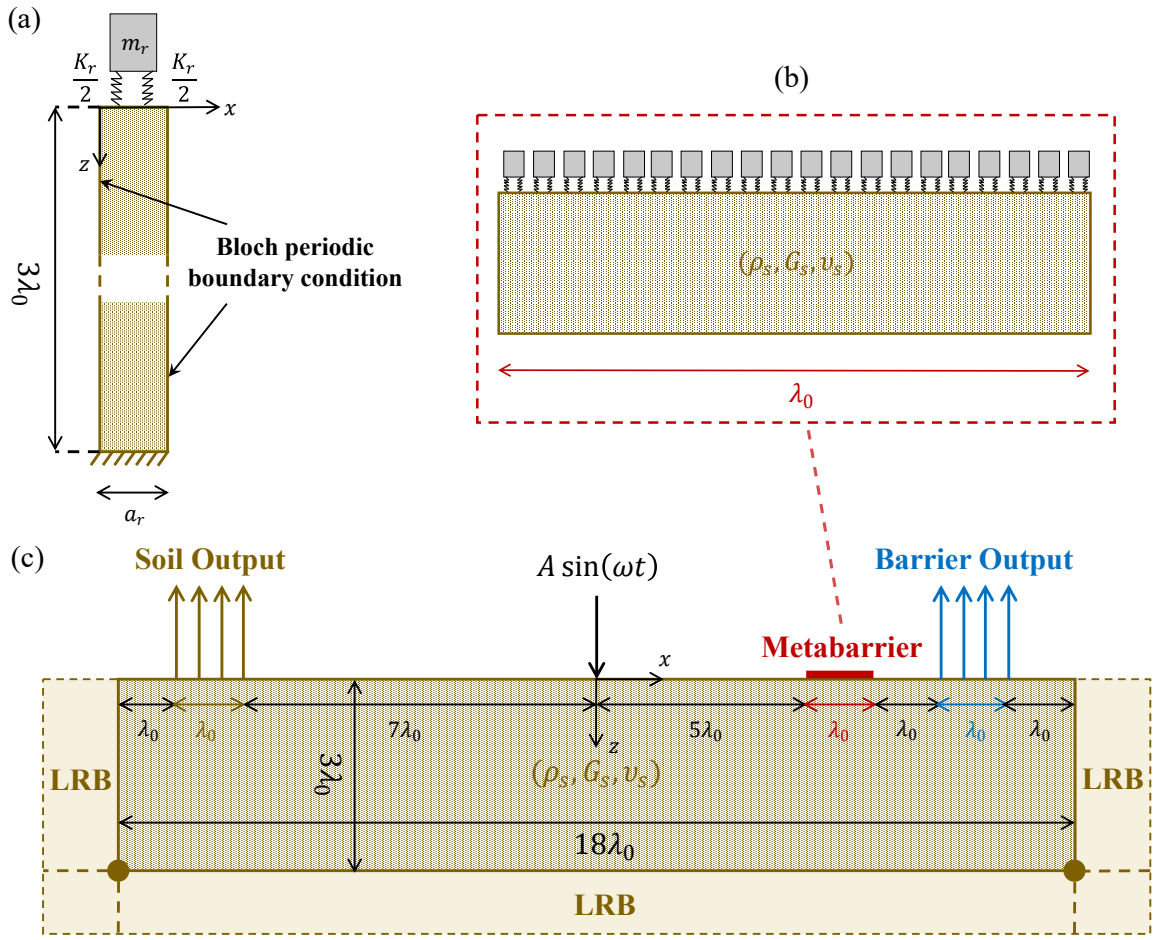

Figure 3: Schematics of the seismic metabarrier FE model. (a) A representative unit-cell of the metabarrier. (b) An array of 20 resonators forms the metabarrier. (c) The 2-D wavefield model used to calculate the Transmission Coefficient (TC).

To quantify the seismic isolation performance of the barrier, one can either perform a time-history analysis and measure the soil response via Fourier transform (Zeighami et al., 2021b) or perform harmonic analysis to explicitly obtain the result in the frequency domain (Palermo et al., 2018b). In this study, we employ the latter approach (i) to understand the physics of the problem by evaluating the transmission/attenuation performance of the metabarrier at different frequencies and comparing the results with their counterparts obtained from the dispersion analysis and (ii) to minimize the computational cost of simulations. In this context, a harmonic displacement excites the model from the center to evaluate the Transmission Coefficient (TC) and Attenuation Coefficient (AC) of the metabarrier (Palermo et al., 2018b) as:

$$TC(f) = \frac{\int_0^{L_{out}} |v_b| dx}{\int_0^{L_{out}} |v_s| dx}, \quad AC(f) = 1 - TC(f), \tag{3a-b}$$

where v_b is the vertical nodal displacement of the soil measured from barrier output (see Fig. 3c), to be averaged over the output length L_{out}, and v_s is the same quantity evaluated from the reference soil in the absence of the metabarrier.

2.4. Uncertain model parameters

During the design and implementation phases of a seismic metabarrier, the out-of-plane depth (l_r) and the resonators spacing (a_r) are typically considered as deterministic parameters. The mass (m_r) and stiffness (K_r) of the resonator can be regarded as uncertain parameters due to manufacturing imperfections in their geometries or weight differences. To streamline the analysis, we consider mass as the only uncertain parameter of the resonator, since the mass per unit area ratio ($m_r/(a_r l_r)$) in Eq. (1) controls the hybridization of the fundamental surface mode (Palermo et al., 2016). Regarding the mechanical parameters of the soil, these data are generally obtained from experiments. Thus, their estimates are typically uncertain, even for homogeneous and isotropic geomaterials. Since the variation of the Poisson ratio (ν_s) is generally less pronounced than variations of mass density (ρ_s), and given that the shear modulus (G_s) is related to ν_s via the Young modulus (E_s), we consider ρ_s and G_s as the uncertain parameters of the soil and set ν_s as a deterministic parameter. In summary, the uncertain model parameters of the present study are ρ_s, G_s, and m_r.

To rigorously assess the significance of uncertain parameters on the isolation properties of metabarriers, we consider three common soil scenarios found in nature.

We assume that such soils have homogeneous mechanical properties throughout the depth of the elastic waveguide. The soil types are (*i*) sedimentary soil (S1), (*ii*) completely weathered granite (S2), and (*iii*) silty-clay soil (S3). These soil types are not ideal for construction purposes and require engineering intervention to increase their bearing capacities. Sedimentary soils are loose sediments usually found near river basins. Weathered granite soils are found in mountainous areas where infrastructures (dams, mountain roads, and railways) are built. Silty clay soil is an intermediate between sandy and clay soils that tends to shift due to moisturizing/drying; therefore, they require deep foundations to protect the infrastructures against seismic action.

In this study, the uncertain model parameters are considered independent and identically distributed random variables, each characterized by a uniform distribution within the intervals listed in Table 1. The choice of the latter distribution enables one to give the same weight to all parameter values across their support. We assume that the ranges of the variability of ρ_s and G_s are centered around the values experimentally found by Cai et al. (2021), who documented Rayleigh waves velocities $c_R = [94.91, 64.70, 55.80]$ m/s for S1, S2, and S3, respectively. An effective coupling between the metabarrier and the soil is seen for sedimentary soils with $c_R < 1000$ m/s (Colombi et al., 2016c). Even as values of the soil parameters of the current study (see Table 1) are representative of sedimentary-basins-like (soft) soils with low Rayleigh wave speeds, the sensitivity of the results discussed in Sec. 3 are not strictly limited to these wave velocity ranges, and can be extended in future studies to the soils with average Rayleigh celerity ($300 \leq c_R \leq 500$ m/s).

We consider the uniform distributions of ρ_s and G_s to be characterized by a coefficient of variation of 10% to encompass a range of values typical of common engineering applications. The lower and upper bound of the support associated with the distribution of the resonator mass are defined upon considering a 5% coefficient of variation. The mean value of the resonator mass is assumed to be 1500 kg. We consider a target resonant frequency of $f_r = 5$ Hz for the incoming waves. This, in turn, leads to an axial stiffness of the resonator $K_r = 1480$ kN/m and $\lambda_0 = 19$ m, 13 m, and 11 m for S1, S2, and S3, respectively. Table 1 lists, for each Scenario, the range of variability of the model's uncertain parameters and the value of the deterministic parameters.

2.5. Global sensitivity analysis (GSA)

We employ GSA techniques to diagnose the influence that the uncertainties on model parameters (ρ_s, G_s, m_r) have on the attenuation performance of the metabarrier (measured as TC and evaluated via Eq. 3a). As stated in Section 1, we rely on (*i*) the classical variance-based approach grounded on the evaluation of the well-known

Model parameters			Scenario 1	Scenario 2	Scenario 3
Parameter	Units	CV [%]	Range/Value		
G_s	MPa	10	13.5 - 16.5	9.36 - 11.44	6.14 - 7.50
ρ_s	kg/m^3	10	1350 - 1650	1890 - 2310	1665 - 2035
m_r	kg	5	1425 - 1575	1425 - 1575	1425 - 1575
ν_s	-	-	0.45	0.25	0.32
K_r	kN/m	-	1480		
a_r	m	-	1		
l_r	m	-	1		

Table 1: Ranges of variability for the model uncertain parameters considered in the GSA and values of deterministic model parameters considered in this study. Values of the coefficient of variation of the uncertain model parameters are also listed.

Sobol indices (Saltelli and Sobol', 1995) and (*ii*) the moment-based GSA framework introduced by Dell'Oca et al. (2017).

2.5.1. Variance-based Sobol Indices

Sobol indices (Saltelli and Sobol', 1995) quantify the relative expected reduction of the variance of a target model output due to knowledge of (or conditioning on) an uncertain model parameter. In this context, considering a model output ζ, which depends on P random parameters collected in vector $\boldsymbol{\theta} = (\theta_1, \theta_2, ..., \theta_P)$ and defined within the space $\Gamma = \Gamma_1 \times \Gamma_2 \times ... \times \Gamma_P$ ($\Gamma_p = [\theta_{p,min}, \theta_{p,max}]$ corresponding to the support of the p-th parameter, θ_p), the principal Sobol' index S_{θ_p} associated with a given model parameter θ_p is evaluated as

$$S_{\theta_p} = \frac{V\left[E\left[\zeta|\theta_p\right]\right]}{V\left[\zeta\right]}. \tag{4}$$

Here, $E\left[\cdot\right]$ and $V\left[\cdot\right]$ represent expectation and variance operators, respectively; the notation $\zeta|\theta_p$ denotes conditioning of ζ on a value of θ_p. Note that S_{θ_p} describes the relative contribution to $V[\zeta]$ due to variability of only θ_p. Joint contributions of θ_p with other model parameters included in $\boldsymbol{\theta}$ to the variance of ζ are embedded in the total Sobol indices (details not shown). Note that by relying on Sobol indices to diagnose the relative importance of uncertain model parameters to model outputs one assumes that the uncertainty of a model output is completely characterized by its variance. Thus, even though Sobol indices are characterized by conceptual simplicity and straightforward implementation and use, they provide only limited information about the way variations of model parameters can influence the complete probability

density function (pdf) of model outputs.

2.5.2. Moment-Based AMA Indices

The moment-based GSA approach proposed by Dell'Oca et al. (2017, 2020) rests on the idea that quantifying the effects of model parameter uncertainty on various statistical moments of the ensuing pdf of model outputs can provide an enhanced understanding of model functioning. Dell'Oca et al. (2017) introduce Moment-Based sensitivity metrics (termed AMA indices) according to which one can evaluate the influence of uncertain model parameters on key elements of the model output pdf, as embedded in its associated statistical moments. The AMA indices are defined as follows (Dell'Oca et al. (2017)):

$$\mathrm{AMA}M_{\theta_p} = \frac{1}{|M[\zeta]|} E\left[|M[\zeta] - M\left[\zeta|\theta_p\right]|\right]. \tag{5}$$

Here, $\mathrm{AMA}M_{\theta_p}$ represents the indices associated with a model parameter θ_p and a given statistical moment M of the pdf of model output ζ. For the purpose of our study we focus on the first two moments (i.e., the mean ($M = E$) and the variance ($M = V$)) of the model output pdf. The AMA indices are intended to quantify the relative importance of parameter θ_p on a given statistical moment of ζ. Large values of these indices indicate that $\zeta|\theta_p$ strongly deviates from its unconditional counterpart.

2.6. Surrogate model

To employ the previously described GSA techniques, several evaluations of TC under diverse combinations of ρ_s, G_s, and m_r are required. Such a procedure is impractical in our scenario due to the heavy computational burden associated with the evaluation of TC. One single simulation takes approximately 72 seconds on an Intel Core i7-116G7 @ 2.80GHz with 32GB of Memory. Thus, here we rely on a generalized Polynomial Chaos Expansion (gPCE) surrogate of the full numerical model that allows for reducing the computational time associated with the execution of the GSA technique (Dell'Oca et al., 2017; Sudret, 2008).

In the context of gPCE, a model $g(\boldsymbol{\theta})$ can be expressed as a linear combination of the multivariate polynomials, $\psi_i(\boldsymbol{\theta})$, i.e.,

$$g(\boldsymbol{\theta}) \approx \sum_{i \in \Lambda^{P,D}} \beta_i \psi_i(\boldsymbol{\theta}),$$
$$\psi_i(\boldsymbol{\theta}) = \prod_{p=1}^{P} \psi_p^d(\theta_p). \tag{6}$$

Here, β_i is the coefficient of the i-th term of the model surrogate; $\psi_p^d(\theta_p)$ is a univariate polynomial of order d of the parameter θ_p; and $\Lambda^{P,D}$ is a multi-index containing the indices of all the multivariate polynomials ($\psi_i(\boldsymbol{\theta})$) with degree equal or smaller than the surrogate degree, D, (i.e., multivariate polynomials where $\sum_{p=1}^{P} d \leq D$).

Note that in the context of gPCE the univariate polynomials must satisfy the orthonormality condition, i.e., $E[\psi_p^j \psi_p^k] = \delta_{jk}$, where δ_{jk} is the Kronecker-delta function, $\delta_{jk} = 1$ if $j = k$ and zero otherwise. Multiple families of polynomials satisfy this condition; however, the selection of the suitable family of polynomials is made based on the pdf of the model parameters, which in this study are considered uniform. Thus, the Legendre polynomial family is employed to construct the surrogates.

The construction of a gPCE surrogate requires the evaluation of the surrogate model coefficients, $\beta = \{\beta_i, \forall\ i \in \Lambda^{P,D}\}$, and the selection of the surrogate model degree, D (Sudret, 2008). Regarding the evaluation of β, we rely on least-square minimization (also termed as regression approach). According to this technique, the surrogate coefficients β are those that minimize the mean square error between TC values computed with the full numerical model, $y(\boldsymbol{\theta})$, and the corresponding outputs of the surrogate model. Thus, several full numerical simulations need to be performed in order to estimate the coefficients β. Generally, as the number of full numerical simulations employed for the construction of the surrogate increases, also the accuracy of the surrogate increases. In this study, the maximum admissible computational burden allows us to perform 1233 full model evaluations encompassing an equal number of randomly selected sets of parameters, such sets of parameters are randomly sampled employing a Quasi-Monte Carlo approach which guarantees that the parameter space is sampled uniformly. The evaluation of β is then performed by minimizing

$$\sum_{s=1}^{1233} \left[g(\boldsymbol{\theta}_s) - \sum_{i \in \Lambda^{P,D}} \beta_i \psi_i(\boldsymbol{\theta}_s) \right]^2, \tag{7}$$

where $\boldsymbol{\theta}_s$ is the s-th randomly selected set of the uncertain model parameters.

In our analyses, the selection of D is performed on the basis of an accuracy test of surrogates with degrees varying between 4 and 13. In such a test, the TC of 50 randomly selected sets of parameters (different from the sets of parameters employed for the estimation of β) is evaluated with the numerical model and the surrogate. Then, the mean absolute error between these two quantities is evaluated, and the surrogate associated with the smallest error is selected and employed for the GSA.

3. Results and Discussion

This Section provides the resulting dispersion curves of each soil Scenario analyzed for a single resonator and the transmission coefficients of the entire metabarrier. The accuracy of the surrogate models generated for the GSA is then discussed. Finally, the GSA results are presented, and some conclusions about the impact of uncertain input parameters on the output results are drawn.

3.1. Dispersion analysis results

Analytical dispersion curves for each Scenario from Eq. (1) are depicted in Fig. 4a (solid curves). The dispersion curve highlights the hybridization of the fundamental surface mode around the local resonance of the resonators in two avoided-crossing branches observed in previous studies (Boechler et al., 2013; Palermo et al., 2016; Colquitt et al., 2017). The split of the fundamental mode results in the generation of a low-frequency band gap typical of the local resonance mechanism, where the propagation of seismic surface waves is impeded within this frequency range. Having an identical mass and stiffness of the resonators, a comparison between different soil Scenarios reveals that the dynamic coupling between surface waves and metabarrier is stronger for the silty clay soil (S3). This is due to the lower relative density between resonator and soil, noting that Rayleigh and shear wave velocities are slower for silty clay soil in comparison with other Scenarios. Under this rationale, soil type 3 presents a flattened in-phase branch (lower branch in Fig. 4a) and propagates with higher velocity in the frequency ranges above the band gap, as evidenced by the larger slope of its out-of-phase branch (upper branch in Fig. 4a). The band gap width falls in the interval $f_{BG} = [f_r, f_r(\alpha + \sqrt{\alpha^2+1})]$, where $\alpha = (\pi m_r f_r)/(a_r l_r)\sqrt{(1-C^2)/(\rho_s G_s)}$ is a dimensionless number that relates resonator mass to the soil mass excited by Rayleigh waves at the resonance (Palermo et al., 2016). Consequently, the band gap width is $\Delta f_{BG} = \alpha - 1 + \sqrt{\alpha^2+1}$ which takes the values 0.80, 0.70, and 0.97 Hz for S1, S2, and S3, respectively. The largest band gap is associated with the silty clay soil, having the lowest shear modulus and Rayleigh velocity among all the cases.

We perform a frequency domain analysis of the FE unit-cell model (see Fig. 3a) in the frequency range of 0 to 10 Hz corresponding to Rayleigh wavelengths between

20 to 240 m in Comsol Multiphysics (COMSOL Multiphysics®, 2022) under plane-strain conditions. The simulations are performed for 1233 realization of collocation points as specified in Sec. 3.3, each containing a set of uncertain parameters. The simulation outcomes are averaged for each Scenario and depicted in Fig. 4a. The eigenfrequency solutions of the FE analysis are marked with dots and super-imposed on the analytical dispersion curves. There is a good agreement between the analytical and numerical solutions. Otherwise, it can be noted that the numerical resonant frequencies are shifted toward the lower values. This frequency shift stems from uncertainties associated with the resonator mass or, equivalently, with the resonant frequency, together with a soft soil mechanism that emerged from the inertia difference between the resonator and soil. For heavy resonating masses, the soil acts as a soft spring with the longitudinal stiffness of K_s working in serial configuration with resonators' springs K_r. The equivalent stiffness of the coupled system would be $K_{eq} = K_r K_s/(K_r + K_s) < K_r$. Thus, the numerical resonant frequency will be $f_{r,FE} = 2\pi K_{eq}^{1/2} m_r^{-1/2}$. Since $K_{S3} < K_{S2} < K_{S1}$, the frequency shift is less pronounced for the soft soil S1. The opposite can be observed for S3. The resulting numerical resonant frequencies are $f_{r,FE} = [4.5, 4.4, 4.3]$ Hz for S1, S2, and S3, while $f_{r,AN} = [4.91, 4.78, 4.84]$ Hz correspond to their analytically evaluated counterparts.

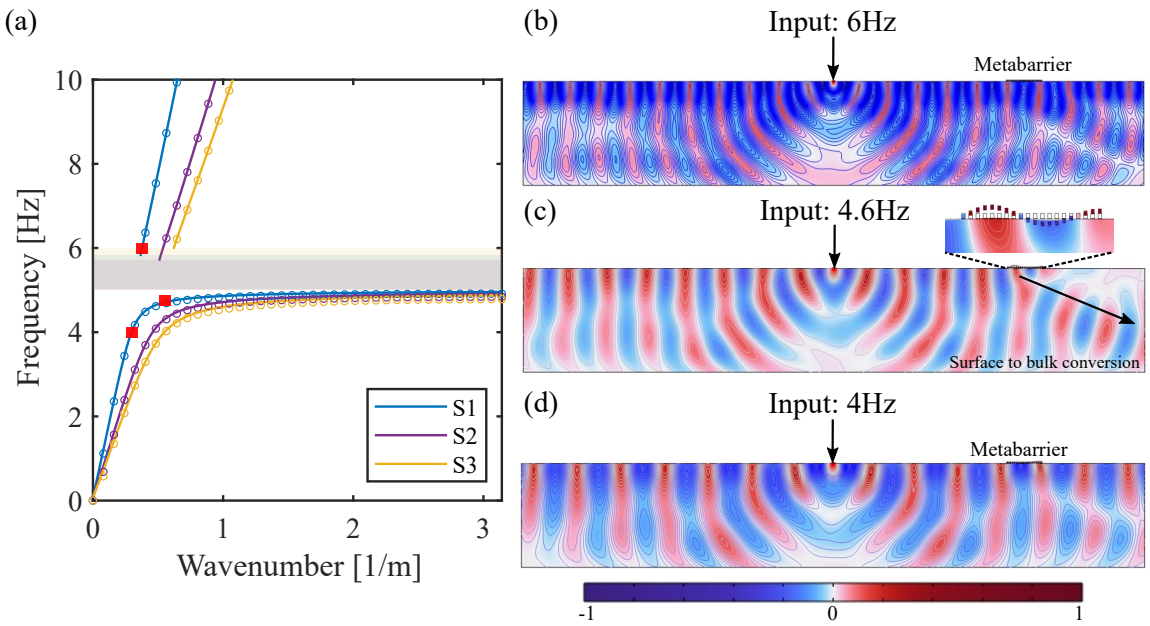

Figure 4: (a) Averaged dispersion curves obtained from the unit-cells of seismic metabarrier for all three Scenarios S1-S3. Analytical surface modes obtained from Eq. (1) are shown with solid lines and FE eigensolutions super-imposed with circles. Highlighted boxes show the band gap region associated with each scenario. The full wavefields are corresponding to (b) out-of-phase surface mode (upper branch the dispersion curve), (c) resonant frequency, and (d) in-phase surface mode (lower branch) of S1. Excitation frequencies are marked with red squares on the dispersion curve.

The full wavefield of the plane-strain FE model (see Fig. 3c) is shown for the out-of-phase and in-phase surface modes of S1 in Fig. 4b and d, respectively. The introduction of the metabarrier (right side of the individual figures) modifies the surface wave propagation compared to the reference soil condition (left side of the figures). The excitation frequencies are denoted with red squares in the dispersion curve of Fig. 4a. For a vertical harmonic excitation with a carrier frequency close to the operational frequency of the metabarrier, the surface-to-shear wave conversion due to the local resonance of the resonators is observed in Fig. 4c. This phenomenon originates from the dynamic interaction between the harmonic motion of seismic surface waves (Rayleigh-like waves) and vertical displacement of resonators inside the barrier (see inset of Fig. 4c). The outcomes of the dispersion relation anticipate a considerable surface wave amplitude reduction around the band gap region. Similar results are obtained for S2 and S3 with minor differences in their numerical resonant frequencies.

3.2. The surface wave attenuation coefficient

We perform a harmonic analysis of the full FE model results of Fig. 3c in the frequency interval of 2 Hz to 7 Hz using a frequency resolution of 0.1 Hz. The triangular mesh elements with identical sizes of the unit-cell model are incorporated in all Scenarios to discretize the models. We obtained TC and AC (Eq. (3)) from the vertical nodal displacements of the barrier output averaged over its length ($L_{out} = \lambda_0$) divided by the same quantity measured from the soil output, as described in Sec. 2.3. Similar to the unit-cell case, we execute the frequency domain simulations for 1233 realization of collocation points and average the outputs of TC and AC for each Scenario. Fig. 5 summarizes the results of the harmonic analysis of the seismic metabarrier.

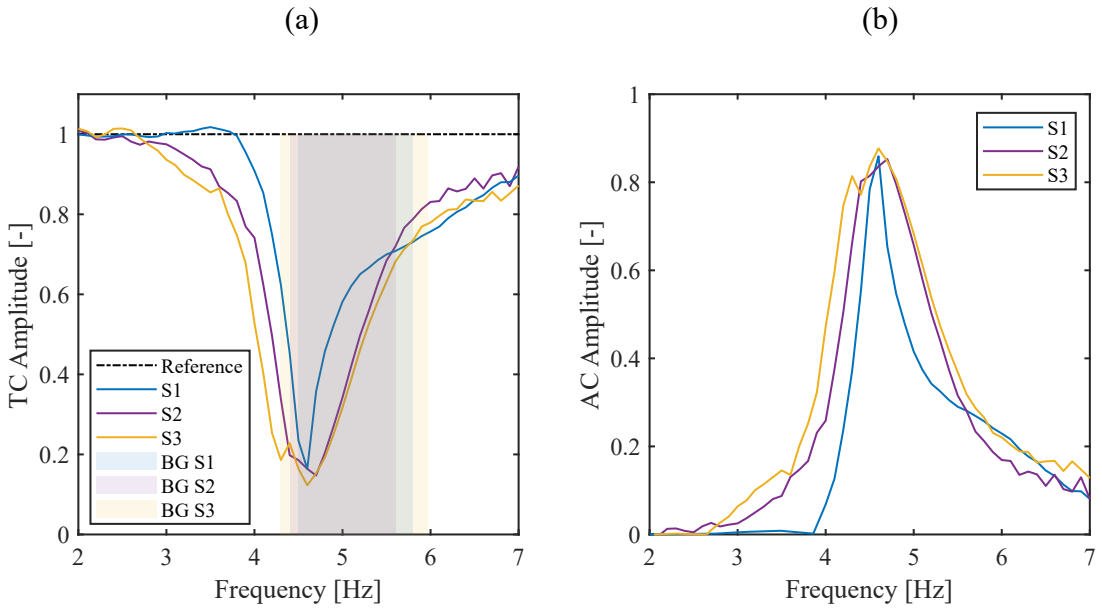

Figure 5: (a) Mean transmission and (b) mean attenuation coefficient of the proposed seismic metabarrier obtained from Eq. (3) in the low-frequency range for all realizations of each Scenario. Shaded areas in Figure 5a represent the band gap (BG) for each Scenario.

The responses of the soils equipped with the resonators are shown with solid lines, while the bare soil response (reference case) is marked with a solid-dashed line. The associated FE band gap regions of each Scenario are highlighted with rectangular boxes. The lower edges of BG zones coincide with the first peak attenuation of each soil model. In all Scenarios, the surface wave attenuation starts around 3 Hz. It becomes more indicative within the BG zone, while the peak attenuation (4.6, 4.7,

and 4.6 Hz for S1, S2, and S3) appears in the proximity of the collective resonant frequencies of the oscillators. In the frequency ranges above the resonance, the transmission/attenuation coefficients present an almost linear increasing/decreasing trend. In the high-frequency regime, the surface wave attenuation in the presence of the metabarrier approaches the reference soil case. The silty-clay soil (S3) is characterized by the broadest attenuation frequency range with the most significant peak analogous to the predictions of the dispersion curve previously discussed in Sec. 3.1. Instead, the soft sedimentary soil (S1) has the narrowest attenuation zone as a result of higher relative density difference and weaker dynamic coupling between the metabarrier and the soil.

3.3. Surrogate models

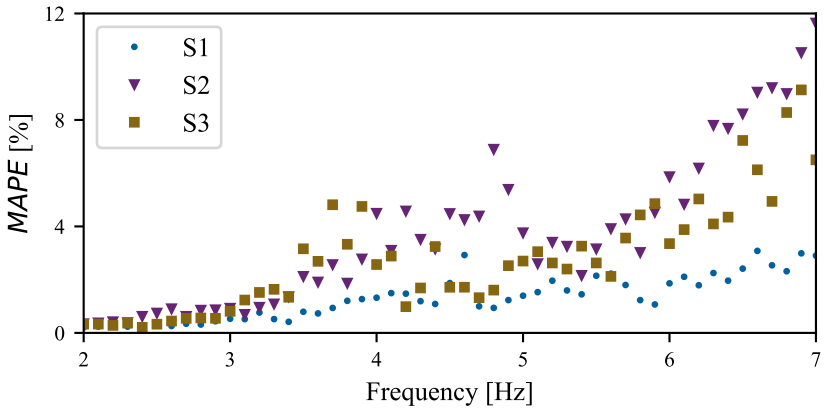

Figure 6: Accuracy of the best surrogate models for diverse frequency values and Scenarios considered in this study.

Fig. 6 presents the accuracy values of the surrogate models constructed for the Scenarios considered in this study. Accuracy is assessed by comparing the results of the surrogate predictions of TC with the results of full numerical simulations; the latter is different from the simulations employed for the surrogate construction. Accuracy is measured with $MAPE$ metric, which is defined as

$$MAPE = \sum_{s=1}^{50} \left[\frac{TC_{surr} - TC_{full}}{TC_{full}} \right]. \tag{8}$$

Note that we construct one surrogate per Scenario and per frequency. Therefore, Fig. 6 presents the accuracy of 153 surrogates. These results show that the accuracy

of the models is generally good ($MAPE \leq 5\%$), except for frequency values larger than 6 Hz. Regarding the different Scenarios, S1 is characterized by the lowest values of $MAPE$, whereas S2 is associated with the largest values.

We construct polynomials of order 12 for the 3 Scenarios. Surrogates of lower polynomial order are associated with reduced accuracy while relying on a higher order was not possible due to the ill-conditioning of the minimization problem required for the evaluation of the surrogate coefficients (details not shown).

3.4. Global sensitivity analysis

The surrogate models obtained in Section 3.3 are evaluated 10^6 times with random combinations of the model parameters. While performing such a task would have required a computational effort of more than two years by employing the full numerical model, relying on the surrogate model considered involves an overall computational time of about 60 seconds on a laptop with an Intel Core i7-8550 @ 1.8GHz with 8GB of Memory. Note that the number of model evaluations is defined to ensure the stability of the sensitivity metrics considered (details not shown). The results of these model evaluations are then employed for the global sensitivity analysis (GSA).

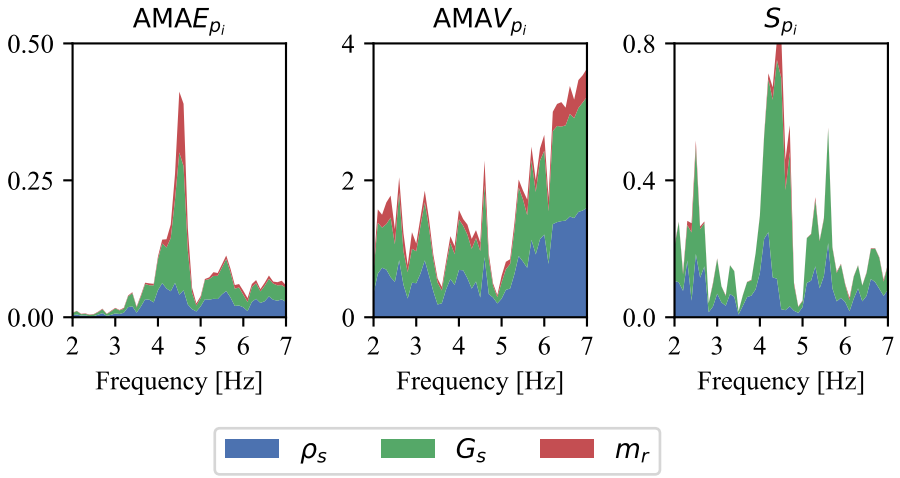

Figure 7: Stacked diagram of the first two moment-based AMA indices (AMAE_{p_i} and AMAV_{p_i}), and Sobol principal indices (S_{p_i}) of the model uncertain parameters considered in this study for Scenario 1.

Fig. 7 depicts the evolution of the first two moment-based AMA indices and the variance-based Sobol indices of the uncertain model parameters of Scenario 1. The results are presented for frequency values in the interval between 2 and 7 Hz, for

which a unique GSA was performed every 0.1 Hz. GSA metrics of ρ_s, G_s, and m_r are depicted in blue, green, and red, respectively. Values of AMAE index indicate that for frequencies below 4 Hz and over 5 Hz, the mean of TC is practically independent of the model parameter values. Conversely, in the interval between 4 Hz and 5 Hz (i.e., the frequency range near the local resonance of the resonators in which the TC/AC assumes minimum/maximum values), knowledge of (or conditioning on) model parameters may significantly modify the mean of TC. In this interval, all uncertain model parameters play an important role in determining the mean of TC, the parameters playing the most and least essential roles being G_s and ρ_s, respectively. This suggests that for 4 Hz$\leq f <$5 Hz, the shear modulus of the soil, which controls the bulk waves velocities and the resonator mass, plays an indispensable role in the definition of the TC mean. For frequency values close to the resonance and due to the effective coupling between resonators and soil, the influence of resonator mass becomes more prominent. Within the band gap frequency range (5 Hz$\leq f \leq$5.8 Hz), the impact of all uncertain model parameters is less pronounced, and resonator mass has the minimum contribution.

Values of the AMAV index suggest that the variance of the model output can be significantly modified by the knowledge of (or conditioning on) a model parameter, such variability being large for high-frequency values. In general, TC variance is governed by G_s and ρ_s. The results of Sobol indices are consistent with those of AMAE and AMAV indices. Sobol indices suggest that the variance of TC can be reduced significantly by the knowledge of (or conditioning on) G_s and ρ_s. The resonator mass (m_r) may play a non-negligible role also for 4 Hz$\leq f <$5 Hz.

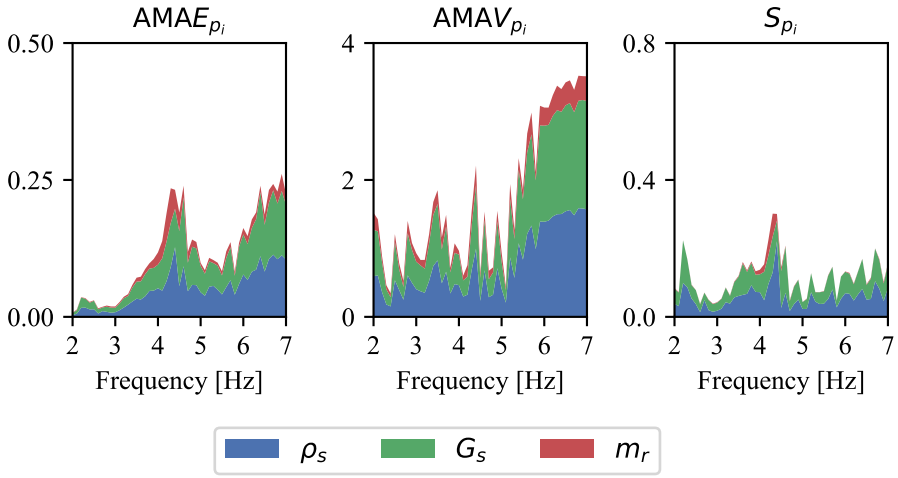

Figure 8: Stacked diagram of the first two moment-based AMA indices (AMAE_{p_i} and AMAV_{p_i}), and Sobol principal indices (S_{p_i}) of the model uncertain parameters considered in this study for Scenario 2.

Fig. 8 presents the evolution of the first two moment-based AMA indices and the variance-based Sobol indices of the uncertain model parameters of Scenario 2. GSA metrics of ρ_s, G_s, and m_r are depicted in blue, green, and red, respectively. Values of AMAE index document that for frequencies below 3 Hz the mean of TC is practically independent of the uncertain model parameter values. Differently from Scenario 1, the knowledge of (or conditioning on) model parameters significantly influences the value of the TC mean for almost all the considered frequencies. The most and least influential parameters are ρ_s and m_r, respectively. Note that the relative importance of ρ_s is close to the relative importance of G_s. m_r has a marginal contribution only in the frequency range between 3.5 Hz and 4.5 Hz, where resonators start moving in phase with the soil domain and ultimately reach the resonance condition. The resonator mass does not have a remarkable impact on the determination of the TC mean outside this frequency interval, and soil parameters govern the overall dynamic behavior of the system. With reference to the AMAV index, the results are similar to those of Scenario 1. This suggests that the variance of the model output can be significantly modified by the knowledge of (or conditioning on) a model parameter, such variability being large for high-frequency values. In general, TC variance is governed by G_s and ρ_s. The results of Sobol indices confirm the outcomes of AMAE and AMAV indices. Sobol indices indicate that the variance of TC can be reduced significantly by the knowledge of (or conditioning on) G_s and ρ_s. As expected, the resonator mass m_r comes into play in the frequency range of 4 Hz$\leq f <$5 Hz.

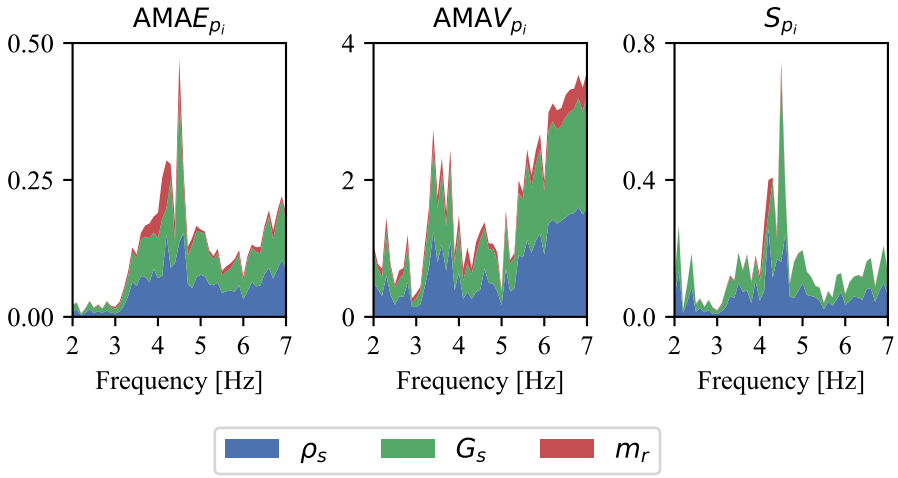

Figure 9: Stacked diagram of the first two moment-based AMA indices (AMAE_{p_i} and AMAV_{p_i}), and Sobol principal indices (S_{p_i}) of the model uncertain parameters considered in this study for Scenario 3.

Fig. 9 presents the same indices as previous Scenarios. GSA metrics of ρ_s, G_s, and m_r are depicted in blue, green, and red, respectively. Similar to the previous cases, the AMAE index values do not depend on the uncertain model parameters in the low-frequency range below 3 Hz. Unlike Scenario 1, the knowledge of (or conditioning on) model parameters considerably influences the values of the TC mean for almost all the considered frequencies. The most and least influential parameters are ρ_s and m_r, respectively. m_r plays a substantial role in the determination of TC mean for 3.5 Hz $\leq f \leq$ 4.5 Hz, close to the frequency range where the maximum ground-motion attenuation is predicted (see Fig. 5a). Regarding AMAV index, the results are similar to Scenario 1, indicating that the variance of the model output can be significantly modified by the knowledge of (or conditioning on) a model parameter, such variability being large for high-frequency values. In general, TC variance is governed by G_s and ρ_s. According to the outcomes of Sobol indices, the variance of TC can be reduced remarkably by the knowledge of (or conditioning on) uncertain soil parameters. The influence of the resonator mass is negligible for the frequency ranges far from resonance. The results of Sobol indices are consistent with those of AMAE and AMAV indices.

The values of the AMAE metric associated with different Scenarios indicate that the mechanical parameters of the soil are more influential than the resonator mass in producing a wider attenuation frequency range for stiff soils such as the weathered granite soil considered in Scenario 3. Such a phenomenon arises from a more

extensive transfer of stress from heavy resonators to the stiff soil and is consistent with the outcomes of the full numerical model (see Fig. 5). Conversely, results of the sensitivity analysis performed for a softer soil like the one considered in Scenario 1 suggest that the resonator mass becomes more dominant only in a narrow frequency range between 4.3 Hz$\leq f \leq$ 4.7 Hz. These results are also consistent with those of the WFEM numerical simulations. Soils of moderate stiffness like the one considered in Scenario 2 present an intermediate case, similar to the results of dispersion analysis and attenuation/transmission coefficients.

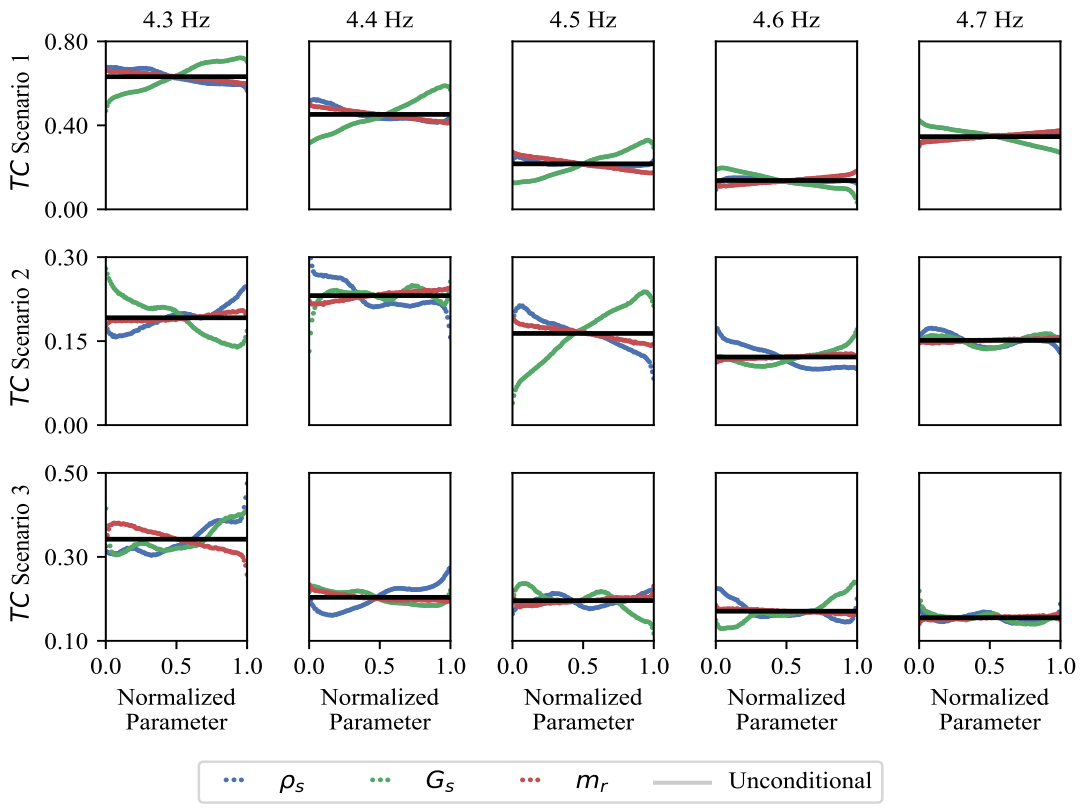

Figure 10: TC conditional on values of the uncertain model parameters considered in this study (ρ_s in blue, G_s in green, and m_r in red). The corresponding unconditional mean is also depicted (black bold horizontal lines). Intervals of variation of the uncertain model parameters are scaled within the unit interval for graphical representation purposes. Results are presented for Scenario 1 (first row), Scenario 2 (second row) and Scenario 3 (third row).

We extend our investigations by analyzing the effect of each uncertain parameter on TC at specific frequency values. Since most of the elastic energy of seismic surface

waves is trapped in the frequency range of 4 Hz$\leq f \leq$6 Hz (see Fig. 5a), we calculate TC values conditioned to values of uncertain model parameters for diverse values of $f = [4.3, 4.4, 4.5, 4.6, \text{and } 4.7]$ Hz where resonant frequencies and frequencies of peak surface wave attenuation can be found for all Scenarios. Fig. 10 presents TC values conditioned to values of ρ_s (in blue), G_s (in green), and m_r (in red). The range of variability of the uncertain parameters is scaled to the unit interval for graphical representation purposes. The unconditional value of TC is also depicted (in black) as a reference.

Fig. 10 indicates that across all 3 Scenarios, at the frequency of maximum attenuation (4.6 Hz, 4.7 Hz, and 4.6 Hz for Scenarios 1, 2, and 3, respectively) the influence of uncertain model parameters on TC is less marked than what can be documented at resonance frequencies (4.5, 4.4, and 4.3 Hz for Scenarios 1, 2, and 3 respectively). At the frequency of maximum attenuation, the influence of m_r on the mean of TC is minute compared to the influence that ρ_s and G_s have on the mean of TC. Instead, the resonator mass becomes more influential in the resonant frequency of all Scenarios. In Scenario 1 the resonator mass has a directly proportional effect on the TC mean (i.e., the larger the values of m_r, the larger the values of TC). Whereas in Scenarios 2 and 3, the influence of m_r on the values of TC is virtually negligible.

4. Conclusions

A seismic metabarrier is a passive barrier composed of locally resonant elements devised to control the propagation of seismic surface waves in the long-wavelength regime. Metabarriers have found application in safeguarding unprotected structures and infrastructures by reducing the ground motion generated from seismic surface waves during an earthquake. The engineering implementation of metabarriers demands detailed knowledge of the uncertain parameters affecting their seismic attenuation capability during their design phase. Within the context of seismic isolation, the current study proposes a rigorous methodology to quantify the impact of the uncertainty associated with system parameters on the seismic attenuation efficiency of a metabarrier.

In this study, we analyze the effect that the uncertainty associated with three parameters driving the physical behavior of a metabarrier (i.e., the mass of resonators m_r, soil density ρ_s, and soil shear modulus G_s) has on its attenuation efficiency. A numerical model is developed to obtain the dispersion relation of the proposed metabarrier; its results coincide with those derived via analytical dispersion curves. A low-frequency band gap typical of the local resonance mechanism appears in the

dispersion curve, where a significant seismic surface wave attenuation is anticipated. The narrowest and widest band gap regions are associated with granite (S2) and silty-clay (S3) soils, respectively. In the latter case, stronger dynamic coupling occurs between the resonators and soil due to their higher relative inertia. A companion full numerical model is developed, and frequency domain analysis is performed to measure the transmission/attenuation coefficients of the metabarrier. The stiffest soil, silty-clay soil of S3, presents the largest peak attenuation with the widest attenuation frequency range. On the contrary, the sedimentary soil (S1) has the narrowest global attenuation with the smallest peak attenuation due to its weak dynamic interaction with heavy resonating masses of resonators; this stems from the soft soil mechanism.

The uncertainty of the transmission coefficient TC (i.e., a measure of the attenuation efficiency of a metabarrier) is governed by the uncertain parameters associated with the mechanical properties of the soil (ρ_s and G_s). The influence that such parameters have on TC varies with the frequency at which Rayleigh waves propagate. In general, for Rayleigh waves oscillating at frequencies close to the resonant frequency of the metabarrier, G_s is the parameter with the largest influence on TC, followed by ρ_s and by m_r, a parameter whose influence is not negligible only for frequencies close to the resonance.

The influence of the resonator mass (m_r) on the attenuation efficiency of the metabarrier depends on the type of soil analyzed. For soft soils (e.g., the soils of Scenario 1 and Scenario 2), an increase in the mass of the resonator enhances the attenuation efficiency of the metabarrier (i.e., decreases TC values) by increasing the relative density of resonators with respect to the soil; whereas for the stiffest soil analyzed in Scenario 3 variations of m_r do not significantly modify the values of TC.

Overall, our approach provides new insights into the design and analysis of locally resonant devices to extend current knowledge of metabarriers in different application areas by including the uncertainties associated with the design parameters. The presented methodology does not include some complexities which might arise during the practical implementation of metabarriers. These include, e.g., soil stratigraphy, the presence of groundwater, and soil bearing capacity failure under heavy resonating masses. Otherwise, our approach, in spite of its simplified assumptions, can still be used as a benchmark for advanced numerical models typically adopted in the context of actual geophysical scenarios. The results of this study can impact several segments of engineering, including earthquake engineering, geotechnical engineering, road and railway traffic, and acoustics. Future extensions of the proposed methodology can be tailored to include dampening effects of soil and resonators, the presence of a water table and (possibly) its dynamics, non-linear effects of the soil, and scenarios

encompassing sedimentary soils characterized by large Rayleigh velocities to assess the shielding efficiency of seismic metabarriers.

CRediT authorship contribution statement

Farhad Zeighami: Conceptualization, Methodology, Software, Data curation, Writing - original draft, Writing - review and editing. **Leonardo Sandoval**: Methodology, Software, Data curation, Writing - original draft, Writing - review and editing. **Alberto Guadagnini**: Conceptualization, Methodology, Writing - review and editing, Supervision. **Vittorio Di Federico**: Conceptualization, Methodology, Writing - review and editing, Supervision, Funding acquisition.

Conflict of interest

The authors declare that they have no conflict of interest. There are no data sharing issues since all numerical information is provided in the figures produced by solving the equations in the paper.

Acknowledgments

V. Di Federico acknowledges support from the University of Bologna through the Ricerca Fondamentale Orientata (RFO) Grant 2021.

Appendix A. Dimensionless analysis of the dispersion relation

This Section provides the dimensionless form of the dispersion law of Eq. (1). We exploit the resonator parameters (m_r, K_r, and a_r) as scales. Hence, we introduce a set of dimensionless parameters as follows:

$$\omega^{'} = \frac{\omega}{K_r^{1/2} m_r^{-1/2}} = \frac{\omega}{\omega_r}, \quad k^{'} = \frac{k}{k_{max}} = \frac{k}{\frac{\pi}{a_r}}, \quad G^{'} = \frac{G_s}{\frac{K_r}{a_r}}, \quad l^{'} = \frac{l_r}{a_r}, \quad \rho^{'} = \frac{\rho_s}{\frac{m_r}{a_r^3}} \approx \frac{\rho_s}{\rho_r}, \tag{A.1}$$

where, $\omega^{'}$ is the angular frequency normalized by the angular resonant frequency of the resonator, $k^{'}$ the wavenumber normalized by the maximum wavenumber at the edge of Brillouin zone, $G^{'}$ the shear modulus normalized by the approximate longitudinal modulus of the resonator, $l^{'}$ the dimensionless shape parameter of the resonator, and $\rho^{'}$ the ratio between the mass density of soil and resonator. The

dimensionless dispersion law is derived by substituting the dimensionless parameters of Eq. (A.1) into Eq. (1) to obtain

$$\begin{aligned}&\left(\omega'^2-1\right)\left[\left(2-\frac{\rho'}{G'}\left(\frac{\omega'}{\pi k'}\right)^2\right)^2-4\sqrt{1-\frac{\rho'}{G'}\left(\frac{C\omega'}{\pi k'}\right)^2}\sqrt{1-\frac{\rho'}{G'}\left(\frac{\omega'}{\pi k'}\right)^2}\right]\\ =&\frac{\rho'\omega'}{l'G'^2}\left(\frac{\omega'}{\pi k'}\right)^3\sqrt{1-\frac{\rho'}{G'}\left(\frac{C\omega'}{\pi k'}\right)^2}.\end{aligned} \tag{A.2}$$

In the original dispersion equation of Eq. (1) and taking into account Eq. (2), the angular frequency is an implicit function of eight parameters, i.e. $\omega = fun(k, K_r, m_r, a_r, l_r, \rho_s, G_s, \nu_s)$, while in the dimensionless equation, the dimensionless angular frequency is an implicit function of five parameters, including i.e. $\omega' = fun(k', l', \rho', G', \nu')$. This is in agreement with the Buckingham π theorem, stating that the original dispersion law with $n = 8$ dimensional physical variables can be written in a dimensionless format using $p = n - m = 5$ pure numbers, where $m = 3$ is the number of dimensionally independent scales, chosen to coincide with the variables describing the resonator. As an alternative to the procedure adopted in the main body of the paper, GSA could be performed on Eq. (A.2), where the number of model parameters is reduced.

References

Basone, F., Wenzel, M., Bursi, O.S., Fossetti, M., 2019. Finite locally resonant metafoundations for the seismic protection of fuel storage tanks. Earthquake Engineering & Structural Dynamics 48, 232–252. doi:https://doi.org/10.1002/eqe.3134.

Bianchi Janetti, E., Guadagnini, L., Riva, M., Guadagnini, A., 2019. Global sensitivity analyses of multiple conceptual models with uncertain parameters driving groundwater flow in a regional-scale sedimentary aquifer. Journal of Hydrology 574, 544–556. doi:https://doi.org/10.1016/j.jhydrol.2019.04.035.

Boechler, N., Eliason, J.K., Kumar, A., Maznev, A.A., Nelson, K.A., Fang, N., 2013. Interaction of a contact resonance of microspheres with surface acoustic waves. Phys. Rev. Lett. 111, 036103. doi:https://doi.org/10.1103/PhysRevLett.111.036103.

Boutin, C., Roussillon, P., 2006. Wave propagation in presence of oscillators

on the free surface. International Journal of Engineering Science 44, 180–204. doi:https://doi.org/10.1016/j.ijengsci.2005.10.002.

Brillouin, L., 1946. Wave propagation in periodic structure. McGraw-Hill,, New York, NY.

Brûlé, S., Javelaud, E.H., Enoch, S., Guenneau, S., 2014. Experiments on seismic metamaterials: Molding surface waves. Phys. Rev. Lett. 112, 133901. doi:https://doi.org/10.1103/PhysRevLett.112.133901.

Cai, C., Gao, L., He, X., Zou, Y., Yu, K., Wu, D., 2021. The surface wave attenuation zone of periodic composite in-filled trenches and its isolation performance in train-induced ground vibration isolation. Computers and Geotechnics 139, 104421. doi:https://doi.org/10.1016/j.compgeo.2021.104421.

la Cecilia, D., Porta, G.M., Tang, F.H., Riva, M., Maggi, F., 2020. Probabilistic indicators for soil and groundwater contamination risk assessment. Ecological Indicators 115, 106424. doi:https://doi.org/10.1016/j.ecolind.2020.106424.

Cheng, Z., Shi, Z., 2013. Novel composite periodic structures with attenuation zones. Engineering Structures 56, 1271–1282. doi:https://doi.org/10.1016/j.engstruct.2013.07.003.

Cheng, Z., Shi, Z., Palermo, A., Xiang, H., Guo, W., Marzani, A., 2020. Seismic vibrations attenuation via damped layered periodic foundations. Engineering Structures 211, 110427. doi:https://doi.org/10.1016/j.engstruct.2020.110427.

Colombi, A., Colquitt, D.J., Roux, P.P., Guenneau, S., Craster, R.V., 2016a. A seismic metamaterial: The resonant metawedge. Scientific Reports 6, 27717. doi:https://doi.org/10.1038/srep27717.

Colombi, A., Craster, R.V., Colquitt, D., Achaoui, Y., Guenneau, S., Roux, P., Rupin, M., 2017. Elastic wave control beyond band-gaps: Shaping the flow of waves in plates and half-spaces with subwavelength resonant rods. Frontiers in Mechanical Engineering 3, 10. doi:https://doi.org/10.3389/fmech.2017.00010.

Colombi, A., Guenneau, S., Roux, P., Craster, R.V., 2016b. Transformation seismology: composite soil lenses for steering surface elastic Rayleigh waves. Scientific Reports 6, 25320. doi:https://doi.org/10.1038/srep25320.

Colombi, A., Roux, P., Guenneau, S., Gueguen, P., Craster, R.V., 2016c. Forests as a natural seismic metamaterial: Rayleigh wave bandgaps induced by local resonances. Scientific Reports 6, 19238. doi:https://doi.org/10.1038/srep19238.

Colquitt, D., Colombi, A., Craster, R., Roux, P., Guenneau, S., 2017. Seismic metasurfaces: Sub-wavelength resonators and Rayleigh wave interaction. Journal of the Mechanics and Physics of Solids 99, 379–393. doi:https://doi.org/10.1016/j.jmps.2016.12.004.

COMSOL Multiphysics®, 2022. Comsol ab, stockholm, sweden. URL: https://www.comsol.com.

De Falco, A., Resta, C., Sevieri, G., 2021. Sensitivity analysis of frequency-based tie-rod axial load evaluation methods. Engineering Structures 229, 111568. doi:https://doi.org/10.1016/j.engstruct.2020.111568.

De Ponti, J.M., Colombi, A., Riva, E., Ardito, R., Braghin, F., Corigliano, A., Craster, R.V., 2020. Experimental investigation of amplification, via a mechanical delay-line, in a rainbow-based metamaterial for energy harvesting. Applied Physics Letters 117, 143902. doi:https://doi.org/10.1063/5.0023544.

Dell'Oca, A., Riva, M., Guadagnini, A., 2017. Moment-based metrics for global sensitivity analysis of hydrological systems. Hydrology and Earth System Sciences 21, 6219–6234. doi:https://doi.org/10.5194/hess-21-6219-2017.

Dell'Oca, A., Riva, M., Guadagnini, A., 2020. Global sensitivity analysis for multiple interpretive models with uncertain parameters. Water Resources Research 56, 1–20. doi:https://doi.org/10.1029/2019WR025754.

Deymier, P.A., et al., 2013. Acoustic metamaterials and phononic crystals. volume 173. Springer.

Gläser, D., Dell'Oca, A., Tatomir, A., Bensabat, J., Class, H., Guadagnini, A., Helmig, R., McDermott, C., Riva, M., Sauter, M., 2016. An approach towards a FEP-based model for risk assessment for hydraulic fracturing operations. Energy Procedia 97, 387–394. doi:https://doi.org/10.1016/j.egypro.2016.10.030.

Hariri-Ardebili, M.A., Sudret, B., 2020. Polynomial chaos expansion for uncertainty quantification of dam engineering problems. Engineering Structures 203, 109631. doi:https://doi.org/10.1016/j.engstruct.2019.109631.

Huang, J., Shi, Z., 2013. Attenuation zones of periodic pile barriers and its application in vibration reduction for plane waves. Journal of Sound and Vibration 332, 4423–4439. doi:https://doi.org/10.1016/j.jsv.2013.03.028.

Kala, Z., 2011. Sensitivity analysis of steel plane frames with initial imperfections. Engineering Structures 33, 2342–2349. doi:https://doi.org/10.1016/j.engstruct.2011.04.007.

Kanellopoulos, C., Psycharis, N., Yang, H., Jeremić, B., Anastasopoulos, I., Stojadinović, B., 2022. Seismic resonant metamaterials for the protection of an elastic-plastic SDOF system against vertically propagating seismic shear waves (SH) in nonlinear soil. Soil Dynamics and Earthquake Engineering 162, 107366. doi:https://doi.org/10.1016/j.soildyn.2022.107366.

Krödel, S., Thomé, N., Daraio, C., 2015. Wide band-gap seismic metastructures. Extreme Mechanics Letters 4, 111 – 117. doi:https://doi.org/10.1016/j.eml.2015.05.004.

Liu, X., Ren, Y., Song, X., Witarto, W., 2020. A global sensitivity analysis method based on the gauss-lobatto integration and its application in layered periodic foundations with initial stress. Composite Structures 244, 112297. doi:https://doi.org/10.1016/j.compstruct.2020.112297.

Mace, B.R., Manconi, E., 2008. Modelling wave propagation in two-dimensional structures using finite element analysis. Journal of Sound and Vibration 318, 884–902. doi:https://doi.org/10.1016/j.jsv.2008.04.039.

Maznev, A.A., Gusev, V.E., 2015. Waveguiding by a locally resonant metasurface. Phys. Rev. B 92, 115422. doi:https://doi.org/10.1103/PhysRevB.92.115422.

Miniaci, M., Krushynska, A., Bosia, F., Pugno, N.M., 2016. Large scale mechanical metamaterials as seismic shields. New Journal of Physics 18, 083041. doi:https://doi.org/10.1088/1367-2630/18/8/083041.

Mu, D., Shu, H., Zhao, L., An, S., 2020. A review of research on seismic metamaterials. Advanced Engineering Materials 22, 1901148. doi:https://doi.org/10.1002/adem.201901148.

Ni, A., Shi, Z., 2022. Broadband wave attenuation and topological transport in novel periodic pile barriers. Engineering Structures 262, 114378. doi:https://doi.org/10.1016/j.engstruct.2022.114378.

Palermo, A., Krödel, S., Marzani, A., Daraio, C., 2016. Engineered metabarrier as shield from seismic surface waves. Scientific Reports 6, 39356. doi:https://doi.org/10.1038/srep39356.

Palermo, A., Krödel, S., Matlack, K.H., Zaccherini, R., Dertimanis, V.K., Chatzi, E.N., Marzani, A., Daraio, C., 2018a. Hybridization of guided surface acoustic modes in unconsolidated granular media by a resonant metasurface. Phys. Rev. Applied 9, 054026. doi:https://doi.org/10.1103/PhysRevApplied.9.054026.

Palermo, A., Vitali, M., Marzani, A., 2018b. Metabarriers with multimass locally resonating units for broad band Rayleigh waves attenuation. Soil Dynamics and Earthquake Engineering 113, 265–277. doi:https://doi.org/10.1016/j.soildyn.2018.05.035.

Palermo, A., Yousefzadeh, B., Daraio, C., Marzani, A., 2022. Rayleigh wave propagation in nonlinear metasurfaces. Journal of Sound and Vibration 520, 116599. doi:https://doi.org/10.1016/j.jsv.2021.116599.

Pu, X., Palermo, A., Marzani, A., 2021. Lamb's problem for a half-space coupled to a generic distribution of oscillators at the surface. International Journal of Engineering Science 168, 103547. doi:https://doi.org/10.1016/j.ijengsci.2021.103547.

Saltelli, A., Sobol', I.M., 1995. Sensitivity analysis for nonlinear mathematical models: numerical experience (in Russian). Mathematical models and computer experiment 7, 16–28.

Sandoval, L., Riva, M., Colombo, I., Guadagnini, A., 2022. Sensitivity analysis and quantification of the role of governing transport mechanisms and parameters in a gas flow model for low-permeability porous media. Transport in Porous Media 142, 509–530. doi:https://doi.org/10.1007/s11242-022-01755-x.

Sudret, B., 2008. Global sensitivity analysis using polynomial chaos expansions. Reliability Engineering & System Safety 93, 964–979. doi:https://doi.org/10.1016/J.RESS.2007.04.002.

Sun, F., Xiao, L., Bursi, O.S., 2019. Optimal design and novel configuration of a locally resonant periodic foundation (LRPF) for seismic protection of fuel storage tanks. Engineering Structures 189, 147–156. doi:https://doi.org/10.1016/j.engstruct.2019.03.072.

Velarde, J., Kramhøft, C., Sørensen, J.D., 2019. Global sensitivity analysis of offshore wind turbine foundation fatigue loads. Renewable Energy 140, 177–189. doi:https://doi.org/10.1016/j.renene.2019.03.055.

Vetter, C., Taflanidis, A.A., 2012. Global sensitivity analysis for stochastic ground motion modeling in seismic-risk assessment. Soil Dynamics and Earthquake Engineering 38, 128–143. doi:https://doi.org/10.1016/j.soildyn.2012.01.004.

Zaccherini, R., Colombi, A., Palermo, A., Dertimanis, V.K., Marzani, A., Thomsen, H.R., Stojadinovic, B., Chatzi, E.N., 2020a. Locally resonant metasurfaces for shear waves in granular media. Phys. Rev. Applied 13, 034055. doi:https://doi.org/10.1103/PhysRevApplied.13.034055.

Zaccherini, R., Palermo, A., Marzani, A., Colombi, A., Dertimanis, V., Chatzi, E., 2020b. Mitigation of Rayleigh-like waves in granular media via multi-layer resonant metabarriers. Applied Physics Letters 117, 254103. doi:https://doi.org/10.1063/5.0031113.

Zeighami, F., Palermo, A., Marzani, A., 2019. Inertial amplified resonators for tunable metasurfaces. Meccanica 54, 2053–2065. doi:https://doi.org/10.1007/s11012-019-01020-4.

Zeighami, F., Palermo, A., Marzani, A., 2021a. Rayleigh waves in locally resonant metamaterials. International Journal of Mechanical Sciences 195, 106250. doi:https://doi.org/10.1016/j.ijmecsci.2020.106250.

Zeighami, F., Palermo, A., Vratsikidis, A., Cheng, Z., Pitilakis, D., Marzani, A., 2021b. Medium-scale resonant wave barrier for seismic surface waves. Mechanics Based Design of Structures and Machines 49, 1157–1172. doi:https://doi.org/10.1080/15397734.2020.1835487.

Zeng, C., Zhao, C., Zeighami, F., 2022. Seismic surface wave attenuation by resonant metasurfaces on stratified soil. Earthquake Engineering & Structural Dynamics 51, 1201–1223. doi:https://doi.org/10.1002/eqe.3611.

Zhang, Y., Sahinidis, N.V., 2013. Uncertainty quantification in CO2 sequestration using surrogate models from polynomial chaos expansion. Industrial & Engineering Chemistry Research 52, 3121–3132. doi:https://doi.org/10.1021/ie300856p.